VIII International Conference on Computational Methods in Marine Engineering
MARINE 2019
R. Bensow and J. Ringsberg (Eds)

# ON THE IMPORTANCE OF ADVANCED MESH MOTION METHODS FOR WEC EXPERIMENTS IN CFD-BASED NUMERICAL WAVE TANKS

**Christian Windt[1†], Josh Davidson[2], Dominic Chandar[3] and John V. Ringwood[1]**

[1] Centre for Ocean Energy Research, Maynooth University
North Campus, Maynooth, Co. Kildare, Ireland
[†]e-mail: christian.windt.2017@mumail.ie

[2] Department of Fluid Mechanics, Faculty of Mechanical Engineering
Budapest University of Technology and Economics
H-1111 Budapest, Hungary

[3] Institute Of High Performance Computing
1 Fusionopolis Way, #16-16 Connexis North, Singapore 138632

**Key words:** Mesh motion, Overset grids, Numerical wave tank, Control, OpenFOAM

**Abstract.** For the economical operation of wave energy converts (WECs), energy maximising control systems (EMCSs) are included in the device design, introducing large structural motions. During the numerical modelling of WECs in CFD-based numerical wave tanks (NWTs), the structural motions must be explicitly accommodated in the finite volume domain. Using well known mesh morphing methods, large amplitude WEC oscillations may deteriorate the quality of the spatial discretisation, and push the NWT beyond the limits of numerical stability. To overcome this issue, advanced mesh motion methods, such as overset grids, have been developed; however, these methods are rarely used in numerical WEC experiments. To this end, the present paper aims to highlight the importance of advanced mesh motion methods, when modelling WECs under controlled conditions. To furthermore prove the feasibility of the overset method, implemented in the OpenFOAM framework, simulations of an uncontrolled WEC are performed, and results are compared to simulations using the mesh morphing method. It is shown that the overset method has potential to improve CFD-based models of controlled WECs, but, at the expense of increased computational cost.

## 1 INTRODUCTION

Extensive numerical modelling is required during the research and development of WECs, to design cost competitive and durable devices. A range of numerical models, with varying computational cost and fidelity, are available for wave-structure interaction (WSI) problems

[1]. While lower fidelity models, based on linear hydrodynamic modelling techniques, such as boundary element method-based NWTs, are computationally efficient, their accuracy decreases when the amplitude of the waves and the WEC motion increase beyond the validity of the underlying linearising assumptions. In contrast, higher fidelity models, including the relevant non–linear hydrodynamic effects, such as CFD-based numerical wave tanks (CNWTs), remain accurate over a wide range of operational conditions, at the expense of increased computational cost [2].

The relative strengths and weaknesses of the various numerical models can be leveraged for different problems, at different stages of device development. During early stage development, lower-fidelity models are suitable for parametric studies, where a vast number of simulations are required to sweep a broad parameter space. At higher technology readiness levels, the system under investigation becomes more refined and a higher level of accuracy is required to evaluate the performance of the system, e.g. evaluating array effects [3] or EMCSs [4]. The use of a high fidelity model, able to capture all relevant hydrodynamic non–linearities, has been shown to be particularly vital for accurate assessment of EMCSs, which drive the WEC into resonance with the incoming wave field, resulting in large amplitude motions outside the limits in which lower fidelity models are reliable [5, 6].

Although the fidelity of a CNWT is well suited to the evaluation of EMCSs [6], the relatively large amplitude body motions can introduce numerical instabilities due to the required motion of the CFD mesh. A number of different mesh motion methods are available, whose usage and suitability for WEC experiments is reviewed in [7]. Among these, the overset grid method shows particular promise for handling large amplitude, multi-degree of freedom, motions which may occur in WEC experiments. To date, only a relatively small number of CNWT WEC experiments have employed the overset method [8]–[15]. The limited usage of the overset method in the wave energy field can be attributed to (1) the extensively larger computational cost [19], (2) the introduction of numerical errors in a Volume Of Fluid (VOF) environment, such as violation of mass conservation [18], and (3) the limited availability of the algorithm in CFD software. Previously, the overset method was only available in commercial CFD software packages, and initial studies were all implemented in the commercial CFD solver STAR-CCM+ [8]–[13]. However, recently the limitation in (3) has been removed through the code release of the overset method for the open-source CFD toolbox OpenFOAM (OF), making it freely available to a wider user community. Overset grids in OF have been applied to WEC experiments in Windt *et al.* [14] and Chen *et al.* [15].

In a previous study by the authors [14], the performance of the overset implementation in the OF version v1706 has been assessed. Major drawbacks in terms of accuracy of the solution, computational overhead and parallelisation of the solution process were revealed. Since the publication of [14], some updates of the overset method have been implemented and released in OF v1712 and v1812. To this end, the present paper follows two main objectives:

1. Highlight the importance of advanced mesh motion methods, in particular overset grids, for the analysis of WECs in CNWTs, under controlled conditions. While the initial study in [14] only considered simple free decay tests, the case study in this paper presents an optimally controlled, moored, point-absorber WEC device in irregular waves.

2. To investigate the improvements of the overset method, implemented in the latest OF v1812 release, the results of the case study are analysed under the criteria of accuracy and computational overhead, and are compared against results using the conventional mesh morphing method, as well as a second overset implementation, *opera*[1], developed at the Institute Of High Performance Computing, Singapore [16].

The remainder of the paper is organised as follows. First, a brief overview of the dynamic mesh motion methods utilised is given in Section 2. Next, the case study is detailed in Section 3, providing information of the WEC device, the considered test cases, and the optimal control. Section 4 presents the numerical setup for the considered CNWTs, followed by the presentation and discussion of the results in Section 5. Finally, conclusions are drawn in Section 6.

## 2 DYNAMIC MESH MOTION

The mesh morphing and overset mesh motion methods employed in this paper are briefly introduced in this section. For more details, the interested reader is directed to [7] and [14].

### 2.1 Mesh morphing

If grid connectivity should be retained, mesh morphing is the common method to accommodate body motion in the CNWTs. The displacement of the body (boundary) is diffused within the domain, by solving the Laplace equation:

$$\nabla \cdot (k \nabla \mathbf{u}) = 0\,, \tag{1}$$

where $k$ describes the diffusivity and $\mathbf{u}$ the velocity of the moving boundary. The displacement of the body leads to a deformation of single control volumes and careful model setup is required to maintain sufficient grid quality throughout the spatial domain over the course of the simulation [17]. Depending on the implementation, the diffusivity factor, $k$, gives control over the grid quality during mesh deformation. In the OF environment, distance-based diffusivity is employed, where the user specifies an *inner* and *outer* distance, between which mesh deformation is allowed, and prohibited elsewhere.

### 2.2 Overset grids

In the overset method, (at least) two grids (background and body-fitted) are defined, which may arbitrarily overlay each other. The different grids are internally static, thereby retaining their original structure and quality, but can move relative to each other. Transferring information between the grids requires interpolation, which can lead to conservation and convergence issues, and represents the biggest challenge of this method [18]. At each time step, the overset method performs the following sequential steps (1) Identification of hole cells, (2) Identification of fringe cells, (3) Identification of donor cells, and (4) Interpolation between fringe and donor cells.

[1]Note that *opera* works as an additional application in the OF environment and is not a standalone version of OF

## 3 CASE STUDY

To illustrate the importance of utilising advanced mesh motion methods when performing WEC experiments in a CNWTs, and investigate the performance of the overset method implemented in OF v1812 and *opera*, this section presents a case study of a WEC under controlled conditions. Section 3.1 describes the considered WEC, Section 3.2 the input wave, and Section 3.3 the control design.

### 3.1 WEC structure

The WEC structure is chosen based on the Blind Test Series 2 of the Collaborative Computational Project in Wave Structure Interaction (CCP-WSI) [20]. An axisymmetric, cylindrical geometry, featuring a sharp-cornered bottom and a moon-pool is considered (see Figures 1 and 2). All relevant structural dimensions, as well as the mass and inertial properties of the device are shown in Figure 1 and listed in Table 1.

The structure is moored to the tank floor, using a linear spring, with a stiffness of $67\,\mathrm{N\,m^{-1}}$. Based on the spring stiffness, the draft, and the buoyancy properties, a mooring pretension (in equilibrium position) of 31.55N can be measured (see Table 1).

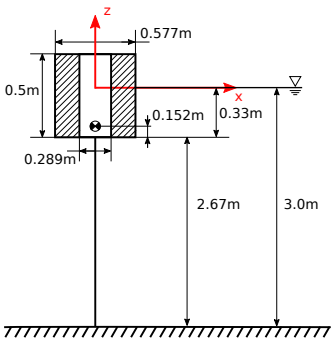


Figure 1: Schematic (not at scale) of the WEC structure

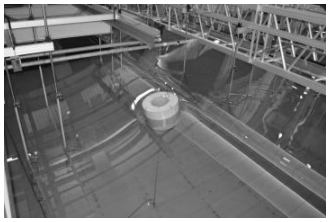

Figure 2: WEC structure in the ocean basin at the COAST Laboratory

Table 1: Properties of the considered WEC structure

| | | |
|---|---|---|
| Mass | [kg] | 61.459 |
| Ixx | [kg m$^2$] | 3.56 |
| Iyy | [kg m$^2$] | 3.56 |
| Izz | [kg m$^2$] | 3.298 |
| Mooring Pretension | [N] | 31.55 |

### 3.2 Input wave

For this case study, an irregular polychromatic JONSWAP sea state with a significant wave height, $H_s$, of 0.25m, and a peak period, $T_p$, of 1.66s, is chosen. According to the linear dispersion relationship, at a water depth, $d$, of 3m, this results in a wave length, $\lambda_p$, of 4.3m. Simulations are run for 66s ($\approx 40\,T_p$). The time trace of the recorded free surface elevation (FSE), measured at the intended WEC location during a preliminary simulation, without the WEC in the CNWT, as well as the according spectral density distribution, are shown in Figure 3.

### 3.3 Optimal control input

In this study, the power take-off (PTO) acts in the heave direction. A PD complex conjugate controller, realised as a linear spring-damper system, is employed. The control force, $u(t)$,

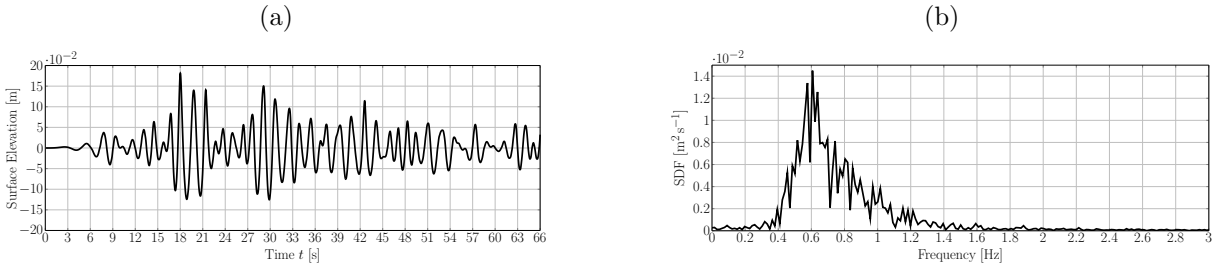


Figure 3: (a) Surface elevation time trace, (b) Spectral density distribution of the FSE signal

follows:

$$u(t) = -b \cdot \dot{x}_{\mathrm{WEC}}(t) - c \cdot x_{\mathrm{WEC}}(t)\,, \tag{2}$$

where $b$ denotes the damping parameter, $c$ is the spring stiffness, and $x_{\mathrm{WEC}}(t)$ and $\dot{x}_{\mathrm{WEC}}(t)$ are the WEC heave position and velocity, respectively. To identify the optimal control parameters, $c$ and $b$, the procedure detailed in [6, 21] is employed. The spring stiffness, $c$, is chosen to shift the uncontrolled resonant period of the WEC, $T_{\mathrm{WEC}}$, in-line with the peak period of the input wave spectrum, $T_p$:

$$c = \frac{k \cdot T_{\mathrm{WEC}}^2}{T_p^2} - k\,, \tag{3}$$

where $k$ is the linear hydrostatic restoring force coefficient of the WEC. The value of $T_{\mathrm{WEC}}$ and $k$ are identified using data from heave free decay test simulations.

To determine $k$, a second-order parametric state-space model is identified, with the transfer function $H(s) = {}^{s}/_{((m+m_\infty)s^2+b_r s+k)}$, optimising the value $k$ to fit the model to an input data set, stemming from the heave free decay test. The required data for the device mass, $m$, is given from the structural properties of the device. The added mass at infinite frequency, $m_\infty$, and the hydrodynamic radiation damping parameter, $b_r$, and calculated using the boundary element method code WAMIT.

Based on the impedance matching control approach, the hydrodynamic radiation damping parameter, at the peak wave period, directly serves as PTO damping parameter $b$ of the PTO.

From this procedure, the optimal control parameters, for the sea state given in Section 3.2, are $b = 37.3\mathrm{N\,s\,m^{-1}}$ and $c = -664\mathrm{N\,m^{-1}}$.

## 4 NUMERICAL WAVE TANK SETUP

In this section, the CNWT setup is detailed. The governing equations are presented (Section 4.1), as well as the treatment of numerical wave generation and absorption (Section 4.2), and the specific details for the three different dynamic mesh motion methods utilised: mesh morphing (Section 4.3), the overset method as implemented in v1812 of OF and *opera* (Section 4.4).

### 4.1 Governing equations

The hydrodynamics in the CNWT are modelled by solving the incompressible Reynold Averaged Navier-Stokes Equations (RANSE), describing the conservation of mass (Equation (4))

and momentum (Equation (5)).

$$\nabla \cdot \mathbf{U} = 0 \qquad (4) \qquad\qquad \frac{\partial \rho \mathbf{U}}{\partial t} + \nabla \cdot \rho \mathbf{U}\mathbf{U} = -\nabla p + \nabla \cdot \mathbf{T} + \rho \mathbf{f}_b \qquad (5)$$

In Equations (4) and (5), $t$ denotes time, $\mathbf{U}$ is the fluid velocity, $p$ the fluid pressure, $\rho$ the fluid density, $\mathbf{T}$ the stress tensor, and $\mathbf{f}_b$, the external forces, such as gravity. The water wave advection is captured via the VOF method, proposed in [22], following:

$$\frac{\partial\, \alpha}{\partial\, t} + \nabla \cdot (\mathbf{U}\alpha) + \nabla \cdot [\mathbf{U_r}\alpha(1-\alpha)] = 0 \qquad (6) \qquad\qquad \Phi = \alpha\Phi_{\text{water}} + (1-\alpha)\Phi_{\text{air}} \qquad (7)$$

where $\alpha$ denotes the volume fraction of water, $\mathbf{U_r}$ is the relative velocity between liquid and gaseous phase [23], and $\Phi$ is a specific fluid quantity, such as density. Laminar flow conditions are assumed for all simulations presented herein.

To measure the FSE, the iso-surface of the volume fraction $\alpha = 0.5$ is recorded throughout the course of the simulation, and can be extracted at specific locations in a post-processing step.

### 4.2 Numerical wave generation & absorption

The IHFOAM [24] toolbox is employed for wave generation and absorption. IHFOAM is readily implemented in OF v1812, and can be classified as a static boundary method [25]. Waves are generated at the up–wave boundary of the CNWT, by prescribing the water level, through the water volume fraction, and the fluid velocity. For an irregular, polychromatic sea state, the wave amplitudes and phases for each frequency component of the wave act as inputs to the wave maker. For wave absorption, a correction velocity, based on the shallow water theory, is imposed at the down–wave domain boundary, to cancel out the incoming wave.

### 4.3 Mesh morphing

In this section, the setup of the CNWT employing mesh morphing will be only described briefly. A detailed description, including convergence studies and investigations into the necessity of turbulence modelling are given in [26].

The CNWT spans a length of $4.9\lambda_p$ (in the x-direction, see Figure 4) and $1.8\lambda_p$ in the y-direction, perpendicular to the wave propagation direction. In the z-direction, the CNWT spans $2d$, where $d$ is the water depth. The still water level is located at $z = 0$. The structure is located $1.7\lambda_p$ down wave from the wave generation boundary, and $3.2\lambda_p$ up wave from the absorption boundary, which refers to $(x, y, z) = (0, 0, 0)$.

The symmetry of the problem is exploited, and a symmetry boundary condition is applied in the xz-plane, at $y = 0$. This enforces constraints on the motion of the device, only allowing translational motion in surge and heave, as well as rotational motion in pitch.

In the free surface interface region, and around the body, the domain is discretised with 10 cells per $H_s$ (in z-direction), featuring an aspect ratio of 2. Towards the down wave boundary of the CNWT, cell stretching is applied to enhance wave absorption and reduce the overall cell count. In the y-direction, cells feature an aspect ration of 1, over a length of $2R$, where $R$ is the device radius. Further away from the structure, cell stretching is applied. The overall cell count

in the domain is 776248. A screen-shot of the spatial discretisation of the CNWT is shown in Figure 4. The field variable $\alpha$, at time $t = 0$, is depicted in Figure 5.

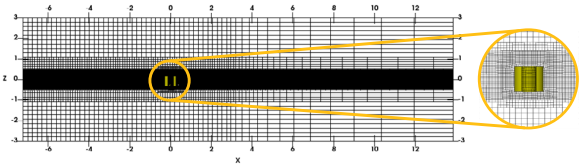

Figure 4: Two-dimensional (2D) slice (xz-plane) of the spatial problem discretisation. The WEC structure is (yellow colour code) is located at $(x, y, z) = (0, 0, 0)$.

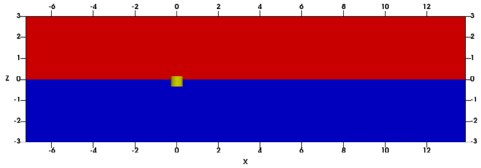

Figure 5: 2D slice (xz-plane) of the CNWT. The water (blue) and air (red) phase are depicted, together with the WEC structure (yellow).

### 4.4 Overset grid

In terms of CNWT setup, the two implementations of the overset method do not differ and the same CNWT can be employed, excepting an alteration between the boundary conditions used to identify overset patches. The setup of the CNWT follows the setup outlined in [14]. The domain comprises a background and an overset mesh (see Figure 6). The dimensions, as well as the spatial discretisation of the background mesh, is virtually the same as for the mesh morphing CNWT, and the symmetry boundary condition is also applied in the xz-plane, at $y = 0$. The overset mesh region (red color code in Figure 6), spans over $1.57R$ x $1.57R$ x $0.88R$ in the x-, z-, and y-directions. The device is located in the centre of the overset mesh. The overall cell count for the overset CNWT is 966766.

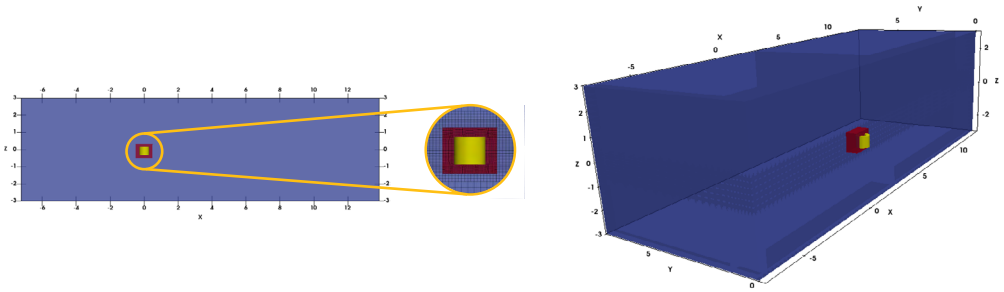

Figure 6: 2D slice (xz-plane) and 3D screen shot of the CNWT for the overset method, where the background mesh is blue, the overset region is red and the WEC structure is yellow.

## 5 RESULTS & DISCUSSION

In this section, the results for four different simulations are presented and discussed. In Section 5.1, results for an uncontrolled versus controlled device, employing the mesh morphing method, are shown. Next, in Section 5.2, results of the uncontrolled device, simulated with mesh

morphing, are compared to the equivalent results from simulation with the two implementations of the overset method.

### 5.1 Uncontrolled vs. controlled

Figure 7 shows the time traces of the surge and heave displacement for the case of an uncontrolled (black solid) and controlled (dashed red) WEC, using the mesh morphing method. For reference, Figure 7 also includes the FSE time trace, at the device location, from the empty tank simulation.

For the case of the uncontrolled WEC, it can be observed that the WEC surges in the wave propagation direction, and oscillates back due to the mooring forces, with a maximum displacement of 1m (from its equilibrium position) at $t = 22$s. In heave, the maximum amplitude is 0.2m (at $t = 30$s) and the overall trajectory is seen to closely follow the FSE. For the case of the controlled device, results are only available up to 22.5s, at which time the simulation aborts, due to poor mesh quality. Larger WEC displacements, in surge and heave, can be observed compared to the uncontrolled device, which can be expected since the EMCS enhances the body motion.

Figure 8 shows screen-shots of the CNWT, for the cases of an uncontrolled and controlled WEC, taken at four different time instances, representing: zero surface elevation ($t = 9$s), maximum positive surface elevation ($t = 18$s), maximum negative surface elevation ($t = 19$s) and the last time instance simulated for the controlled device ($t = 22.5$s). It can readily be seen that the two simulations result in significantly different body motions. At $t = 22.5$s, the mesh in the down wave of the controlled WEC is highly skewed, resulting in the abortion of the simulation.

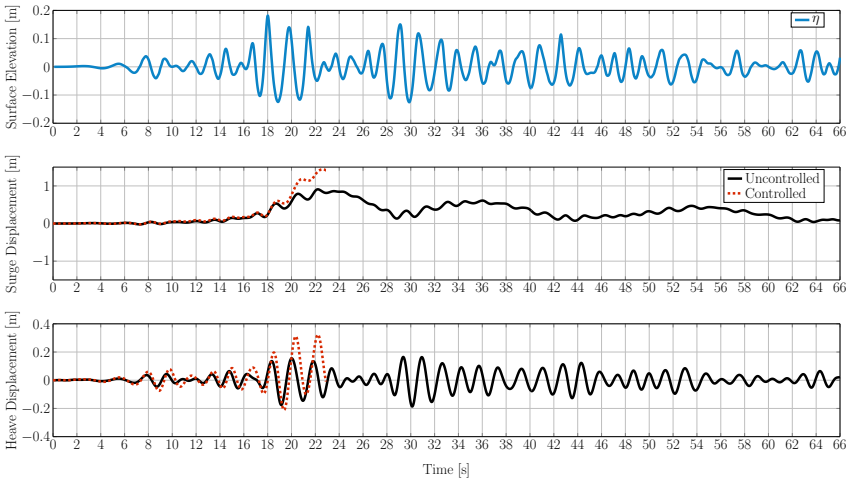


Figure 7: Time traces of the FSE, and the surge and heave displacements of the WEC which are plotted for an uncontrolled (black solid) and controlled (dashed red) device.

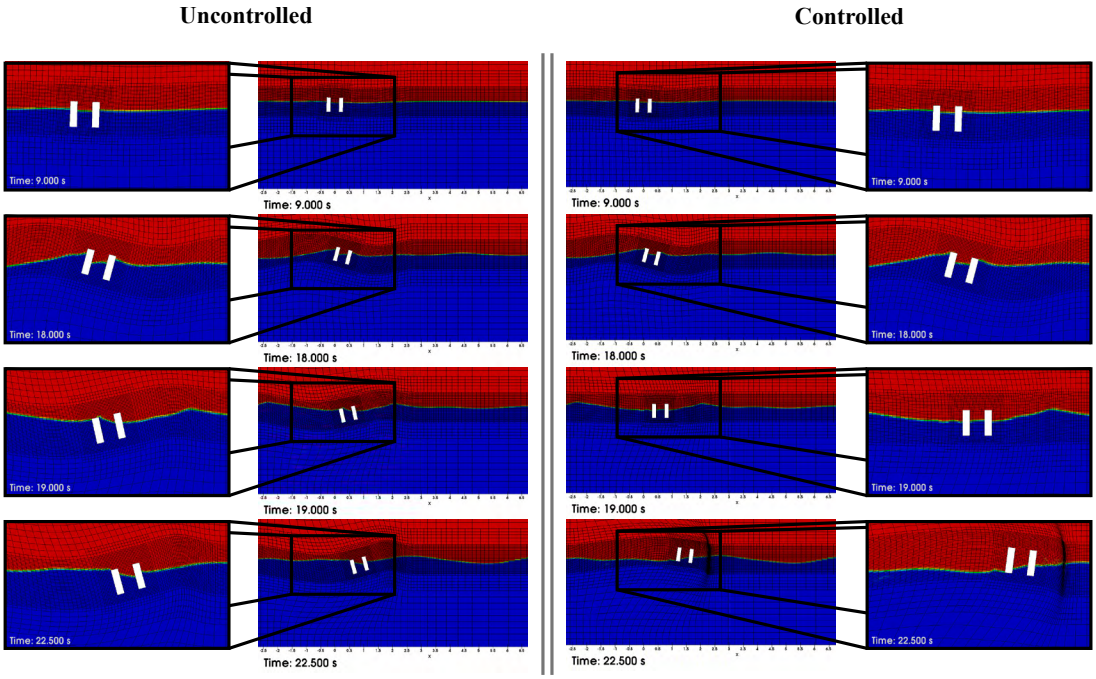


Figure 8: Mesh deformation in the NWT for the mesh morphing method. After 22.5s, the simulation of the controlled WEC aborts, due to poor mesh quality.

### 5.2 Mesh morphing vs. overset grids

The results in Section 5.1 highlight the importance of advanced mesh motion methods, when modelling WECs under controlled conditions. To evaluate the feasibility of the overset method, as an alternative to mesh morphing, the uncontrolled device is modelled, using the overset method, as implemented in OF v1812 and *opera*, and results are compared to the mesh morphing method. Figure 9a shows the time traces of the surge and heave displacement for the mesh morphing (black solid) and overset grid (v1812) (dashed red) methods. To quantify the agreement between the mesh morphing and overset method, the Mean Average Percentage Errors (MAPEs) (see Equation (8)) are evaluated. In Equation (8), $n$ is the number of samples, $y_i$ denotes the data of the mesh morphing method and $\tilde{y}_i$ the data of the overset method. To compare the relative computational efficiency of the dynamic mesh motion methods, the normalised runtime $\Delta t_{\mathrm{r,n}}$ is employed, following Equation (9). In Equation (9), $t_{\mathrm{s,MM}}$ and $t_{\mathrm{r,MM}}$ denote the simulated time and required run time of the mesh morphing method, while $t_{\mathrm{s,OSG}}$ and $t_{\mathrm{r,OSG}}$ denote the simulated time and required run time of the overset method.

$$\mathrm{MAPE} = \frac{1}{n}\sum_{i=1}^{n}\left(\frac{y_i - \tilde{y}_i}{y_i}\right)\cdot 100\% \qquad (8)$$

$$\Delta t_{\mathrm{r,n}} = \frac{t_{\mathrm{s,MM}}/t_{\mathrm{r,MM}}}{t_{\mathrm{s,OSG}}/t_{\mathrm{r,OSG}}} \qquad (9)$$

A relatively good match between the mesh morphing and the overset method (v1812) can be observed, with MAPEs of $\mathrm{MAPE}_{\mathrm{Surge}} = 9.2\%$ and $\mathrm{MAPE}_{\mathrm{Heave}} = 0.5\%$. For the results of the overset method (*opera*) (see Figure 9b), a similarly good match with the mesh morphing can be observed, with $\mathrm{MAPE}_{\mathrm{Surge}} = 5.7\%$ and $\mathrm{MAPE}_{\mathrm{Heave}} = 0.3\%$.

In terms of computationally efficiency, the normalise runtime, $\Delta t_{\mathrm{r,n}} = 3.7$ for the implementation in v1812, and $\Delta t_{\mathrm{r,n}} = 2.6$ for the implementation in *opera*, indicate an overall longer computation time for the overset method, compared to mesh morphing, which is consistent with findings in [14] and [15]. Furthermore, it can be observed that the implementation of the overset method in *opera* is computationally more efficient, compared to the implementation in v1812.

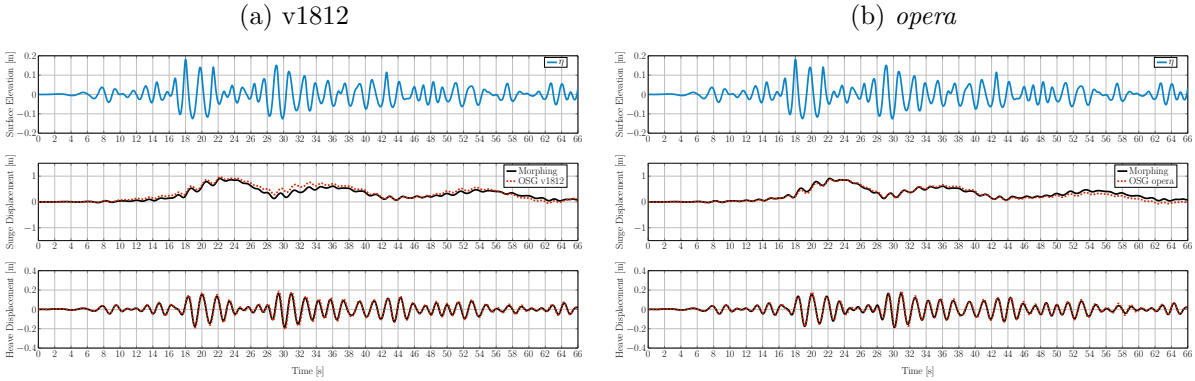


Figure 9: Time traces of the FSE, and the surge and heave displacement of the uncontrolled WEC, for the mesh morphing (black solid) and overset (dashed red) methods.

## 6 CONCLUSIONS

This paper present the modelling of a WEC device, using two different dynamic mesh motion methods. Comparing the results for the uncontrolled and controlled WEC device, when considering mesh morphing, highlights the importance of advanced mesh motion method, for the modelling of WECs under controlled conditions.

Overset grids prove to be a feasible alternative, showing potential for the analysis of WECs under controlled conditions, by avoiding the deterioration of the mesh quality. In the light of the results found in [14], significant improvements can be observed in the current release of the overset method in v1812, in terms accuracy and computational efficiency, compared to the initial release in v1706. Although the implementation of the overset method in *opera* proves to be of slightly higher accuracy and computational efficiency, compared to the implementation in v1812, the computational expense for overset methods is still significantly higher, compared to the mesh morphing method.

## ACKNOWLEDGEMENTS

This paper is based upon work supported by Science Foundation Ireland under Grant No. 13/IA/1886. Josh Davidson is supported by the Higher Education Excellence Program of the Ministry of Human Capacities in the frame of Water science & Disaster Prevention research area of Budapest University of Technology and Economics (BME FIKP-VÍZ). Dominic Chandar is supported by the Institute Of High Performance Computing, Singapore.

## REFERENCES


[1] Penalba, M. and Giorgi, G. and Ringwood, J.V. Mathematical modelling of wave energy converters: a review of nonlinear approaches. *Renewable and Sustainable Energy Reviews* (2017) **78**:1188–1207.

[2] Folley, M. *Numeircal Modelling of Wave Energy Converters*. Academic Press (2016).

[3] Ruehl, K. and Bull, D. Wave Energy Development Roadmap: Design to commercialization. *OCEANS 2012 MTS/IEEE: Harnessing the Power of the Ocean* (2012) **78**:1188–1207.

[4] Ringwood, J.V. and Bacelli, G. and Fusco, F. Energy-maximizing control of wave-energy converters: The development of control system technology to optimize their operation. *IEEE Control Systems* (2014) **34**:30–55.

[5] Giorgi, G. and Penalba, M. and Ringwood, J.V. Nonlinear Hydrodynamic Models for Heaving Buoy Wave Energy Converters. *in the Proceedings of the 3rd Asian Wave and Tidal Energy Conference, Marina Bay Sands, Singapore* (2016).

[6] Davidson, J. and Windt, C. and Giorgi, G. and Genest, R. and Ringwood, J.V. Chapter: Evaluation of energy maximising control systems for wave energy converters using OpenFOAM. *OpenFOAM - Selected papers from the 11th workshop, Guimaraes* (2018).

[7] Windt, C. and Davidson, J. and Ringwood, J.V. High-fidelity numerical modelling of ocean wave energy systems: A review of CFD-based numerical wave tanks. *Renewable and Sustainable Energy Reviews* (2018) **93**: 610–630.

[8] Stansby, P. and Gu, H. and Moreno, E.C. and Stallard, T. Drag minimisation for high capture width with three float wave energy converter M4. *in the Proceedings of the 11th European Wave and Tidal Energy Conference, Nantes* (2015).

[9] Bharath A. and Penesis, I. and Nader, R.R. and Macfarlane, G Non-Linear CFD Modelling of a Submerged Sphere Wave Energy Converter. *in the Proceedings of the 3rd Asian Wave and Tidal Energy Conference, Singapore* (2016).

[10] Coiro, D.P. and Troise, G. and Calise, G. and Bizzarrini, N. Wave energy conversion through a point pivoted absorber: Numerical and experimental tests on a scaled model. *Renewable Energy* (2016) **87**:317–325.

[11] Lu, X. and Denver, D. and Chandar, J. and Chen, Y. and Lou, J. An overlapping domain decomposition based near-far field coupling method for wave structure interaction simulations. *Coastal Engineering* (2017) **126**:37–50.

[12] Elhanafi A, and Macfarlane, G. and Fleming, A. and Leong, Z. Experimental and numerical investigations on the hydrodynamic performance of a floating-moored oscillating water column wave energy converter. *Applied Energy* (2017) **205**:369–390.

[13] Elhanafi A, and Macfarlane, G. and Fleming, A. and Leong, Z. Experimental and numerical investigations on the intact and damage survivability of a floating-moored oscillating water column device. *Applied Ocean Research* (2017) **68**:276–292.

[14] Windt, C. and Davidson, J. and Akram, B. and Ringwood, J.V. Performance assessment of the overset grid method for numerical wave tank experiments in the OpenFOAM environment. *in the Proceedings of the 37th International Conference on Ocean, Offshore and Arctic Engineering, Madrid* (2018) V010T09A006-1–V010T09A006-10.

[15] Chen, H. and Qian, L. and Ma, Z. and Bai, W. and Li, Y. and Causon, D. and Mingam, C. Application of an overset mesh based numerical wave tank for modelling realistic free-surface hydrodynamic problems. *Ocean Engineering* (2019) **176**:97–117.

[16] Chandar, D.D.J. On overset interpolation strategies and conservation on unstructured grids in OpenFOAM. *in press in Computer Physics Communications* (2019).

[17] Ingram, D.M. and Causon, D.M. and Mingham, C.G. Developments in Cartesian cut cell methods. *Mathematics and Computers in Simulation* (2003) **61**:561–572.

[18] Ferziger, J.H. and Peric, M. *Computational Methods for Fluid Dynamics*. Springer (2001).

[19] Jung, M.S. and Kwon O.J. A Parallel Unstructured Overset Mesh Technique for Unsteady Flow Simulations. *in the Proceedings of the 4th International Conference on Computational Fluid Dynamics ICCFD, Ghent* (2006).

[20] CCP-WSI website Focused wave interactions with floating structures: Blind Test Series 2. `https://www.ccp-wsi.ac.uk/blind_test_series_2` Last accessed 10/12/2018.

[21] Davidson, J. and Giorgi, S. and Ringwood, J.V. Linear parametric hydrodynamic models for ocean wave energy converters identified from numerical wave tank experiments. *Ocean Engineering* (2015) **103**:31–39.

[22] Hirt, C.W. and Nichols, B.D. Volume of Fluid (VOF) Method for the Dynamics of Free Boundaries. *Journal of Computational Physics* (1981) **39**:201–225.

[23] Berberović, E. and van Hinsberg, N.P. and Jakirlić, S. and Roisman, I.V. and Tropea, C. Drop impact onto a liquid layer of finite thickness: Dynamics of the cavity evolution. *Physical Review E* (2009) **79**:036306-1–036306-15.

[24] Higuera, P. and Lara, J.L. and Losada, I.J. Simulating coastal engineering processes with OpenFOAM®. *Coastal Engineering* (2013) **71**:119–134.

[25] Windt, C. and Davidson, J. and Schmitt, P. and Ringwood, J.V. On the assessment of numerical wave makers for CFD simulations. *Journal of Marine Science and Engineering* (2019) **7**:47.

[26] Windt, C. and Davidson, J. and Schmitt, P. and Ringwood, J.V. Contribution to the CCP-WSI Blind Test Series 2: CFD-based numerical wave tank experiments employing an impulse source wave maker. *Submitted to the 13th European Wave and Tidal Energy Conference, Naples* (2019).